Title
Evaluation on material behaviors of pultruded glass fiber reinforced polymer (GFRP) laminates

Journal
Composite Structures, 182

ISSN
0263-8223

Authors
Xin, Haohui
Liu, Yuqing
Mosallam, Ayman S
et al.

Publication Date
2017-12-01

DOI
10.1016/j.compstruct.2017.09.006

Peer reviewed

Composite Structures 182 (2017) 283–300

Contents lists available at ScienceDirect

Composite Structures

journal homepage: www.elsevier.com/locate/compstruct

Evaluation on material behaviors of pultruded glass fiber reinforced polymer (GFRP) laminates

Haohui Xin [a], Yuqing Liu [a,*], Ayman S. Mosallam [b], Jun He [c], Ao Du [a,d]

[a] Department of Bridge Engineering, Tongji University, Shanghai, China
[b] Department of Civil and Environment Engineering, University of California, Irvine, CA, USA
[c] School of Civil Engineering, Changsha University of Science & Technology, Hunan, China
[d] Department of Civil and Environment Engineering, Rice University, TX, USA

ARTICLE INFO

Article history:
Received 28 June 2017
Revised 21 August 2017
Accepted 12 September 2017
Available online 14 September 2017

Keywords:
Glass fiber reinforced polymers (GFRP)
Laminates
Finite element analysis
Pultrusion

ABSTRACT

In order to extend the use of pultruded glass fiber reinforced polymer (GFRP) composite materials in civil engineering, a systematic study on pultruded GFRP laminate is important and realistic for the design and construction of GFRP structures in bridge engineering. A practical method to evaluate the fiber volume fractions and the equivalent thickness of each lamina is proposed considering that a typical pultruded FRP profile is not truly laminated structure in rigorous sense. The elastic modulus and ultimate strength of each lamina were predicted based on micromechanics. In terms of the facts that lack of knowledge of the majority of bridge engineers on the behavior of composites, an innovative carpet plots with different fiber volume fraction are adopted to finish the laminate design procedure without much complicated calculation. In addition, a continuum damage model considering lamina shear nonlinearity, lamina damage along thickness direction, innovative damage evaluation methods, loading/unloading strategy and viscous methods to alleviate the convergence difficulties is proposed and implemented via user material subroutine. Three different types of pultruded GFRP laminate were fabricated, and material properties have been tested to validate the numerical and theoretical models. The Finite element simulation results agreed well with tests and could provide reference for the design and construction of GFRP structures.

1. Introduction

Composite materials combine two or more sub-components together aiming to make up a new material with advantages of each sub-component. The combination of strong fibers and resin binders, generally denoted as fiber reinforced polymer (*FRP*) composites, is one of the most common types. Several applications were reported as main bearing components or strengthening members [1–3] in the field of civil engineering. In terms of cost efficient factors, pultruded glass fiber reinforced polymer (GFRP) composites [4–16] which could meet the established design criteria with reasonable cost is always recommended in the field of bridge engineering.

As is shown in Fig. 1, different from traditional regulated specifications of concrete and steel, FRP composites are inhomogeneous and should be viewed and analyzed at different levels (fiber/resin level, lamina level, laminate level and structure level) and on different scales (micro-mechanics and macro-mechanics). GFRP laminates with different lamina stacking-sequence present different mechanical behaviors and currently there is no specification to provide mechanical properties. The concept that the mechanical performance of GFRP laminates should be designed in multi-scale analysis based on engineering requirement is adopted [16,17]. By changing mechanical performance, angle and thickness of lamina, we could design proper laminates based on the practical requirement.

In the past, several investigations on carbon fiber reinforced polymer (CFRP) for aerospace structures were conducted; however, the results and outcomes of such studies are not generally applicable to composite materials that are commonly used in construction applications such as pultruded composites. Several reasons are listed as below:

(i) As is shown in Fig. 2-a, in aerospace and military applications, advanced manufacturing techniques (e.g. auto clave, SCRIMP, RTM, etc.) and stricter quality control/assurance (QC/QA) procedures are used to produce higher performance composites. In contrast and for economic reasons, as is shown in Fig. 2-b, E-glass fibers are the common type

* Corresponding author.
E-mail address: yql@tongji.edu.cn (Y. Liu).

https://doi.org/10.1016/j.compstruct.2017.09.006
0263-8223/

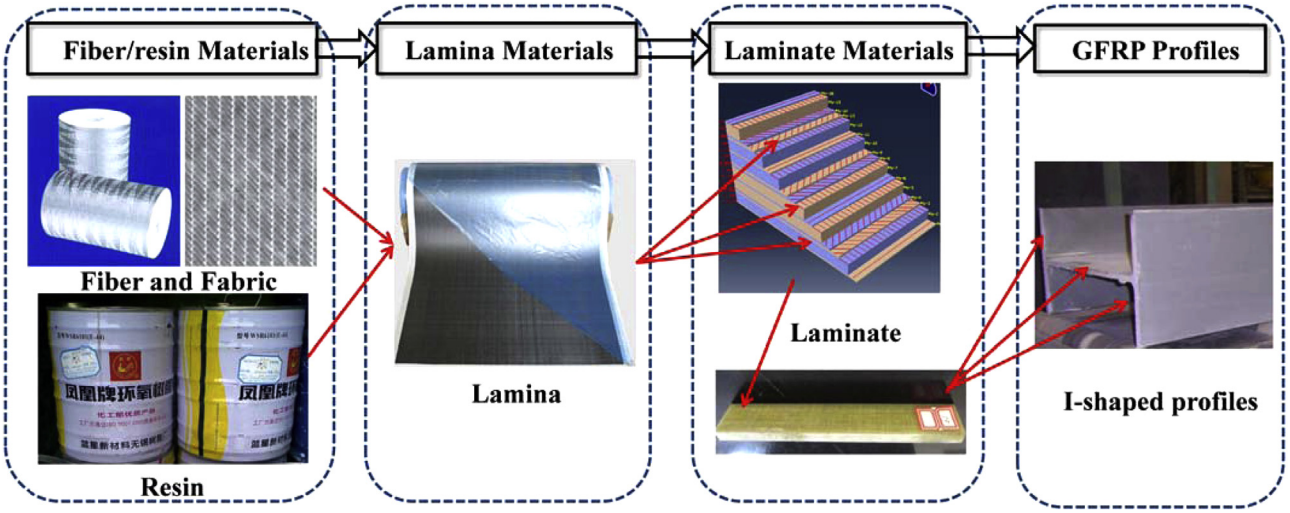

Fig. 1. Different levels of FRP composites.

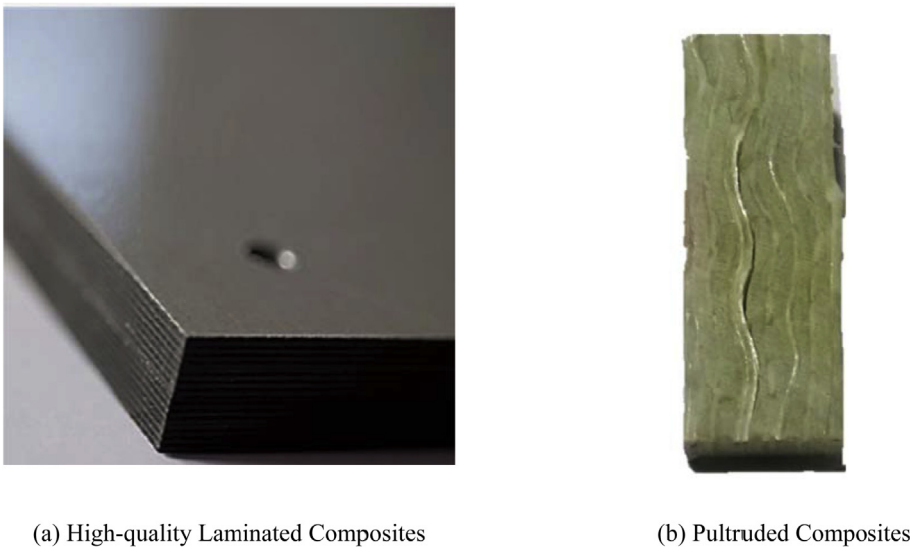

(a) High-quality Laminated Composites (b) Pultruded Composites

Fig. 2. Difference in quality and accuracy of stacking sequence of composite laminates.

reinforcement for the majority of civil engineering applications. The pultrusion process used for producing pultruded profiles for construction application has a relatively lower quality control resulting in uneven and unstable reinforcement distribution. Fabric folds of PFRP perpendicular to pultrusion direction lead to much challenge on the numerical modelling at lamina level.

(ii) As is shown in Fig. 3-a, high quality CFRP laminate in aerospace field includes dozens of lamina forming with pre-impregnated material, different fiber angle is achieved by changing pre-impregnated direction and the thickness of each lamina with different angle is generally identical. However, 0° lamina of pultruded GFRP laminates is made by roving while other angle (i.e. 90°, ±45°) is achieved by fabrics. Due to the limitation of pultrusion manufacture methods, as is shown in Fig. 3-b, the contents of roving is much larger than fabrics for guaranteeing necessary pultrusion traction, leading the thickness of 0° lamina is 5–15 times larger than the laminas with other angle.

(iii) As is shown in Fig. 3, the thickness of pultruded GFRP lamination is generally ten to twenty times larger than CFRP profiles in aircraft system due to low modulus of glass fiber and large load in civil field. The lamina thickness of roving reached 1–2 mm, which is almost same to the thickness of CFRP laminate in aerospace engineering. Thus, the damage/-failure along the thickness direction of roving layer should not be neglected while the thickness effects are generally ignored in classical laminate theory and commercial finite element software. The thickness damage may have small effects on the analysis of whole structure [16,17] but will have larger effects on failure analysis of web-flange junction [7–12] and bolted joints [13,14,18,19].

(iv) The fiber volume fraction and each lamina thickness is not obvious considering that the pultruded FRP members in civil field were not clearly laminated structures in rigorous sense similar to advanced laminated composites in aerospace filed. It is quite difficult and expensive to fabricate pultruded lamina accompany with the pultrusion profiles fabrication for

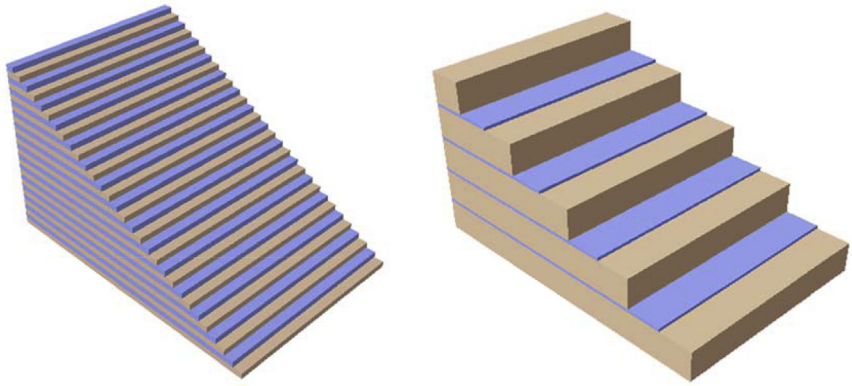

(a) High-quality Laminated Composites (b) Pultruded Composites（equivalent）

Fig. 3. Difference in lamina lay-up of composite laminates.

the ASTM materials characterization tests in order to precisely obtain elastic engineering constants and strengths of each lamina.

(v) Majority of civil engineers lack the knowledge about the behavior, capabilities and limitations (both short- and long-term) of pultrusion; Based on the information obtained from the in-depth literature review, it is believed that there is a dearth of references involving pultruded FRP profiles in civil engineering application with multiscale prediction in both engineering constants and ultimate capacity.

In order to extend the use of pultruded GFRP materials in civil engineering, a systematic study on material properties of GFRP laminates is important and realistic for the design and construction of GFRP structures in civil engineering application. In this paper, considering the facts that lack of knowledge of the majority of civil engineers on the behavior of composites, a carpet plots with different fiber volume fraction are proposed to extend the laminate design procedure without much complicated calculations based on the micro-mechanics and macro-mechanics theoretical analysis. A continuum damage model considering shear nonlinearity, lamina damage along thickness direction, innovative damage evaluation methods, loading/unloading strategy and viscous methods to alleviate the convergence difficulties is proposed and is implemented via user material subroutine. In addition, three different types of pultruded GFRP laminate were fabricated, and material properties have been tested to validate the FE and theoretical models.

2. Design and manufacture of pultruded GFRP laminate

2.1. Laminate lay-up

As shown in Fig. 4, three types of GFRP laminates are fabricated in this paper, namely GF600, GF700 and GF800 with nominal stress of 600, 700 and 800 MPa respectively. The lamina with angle of 0° is fabricated by roving, the lamina with angle of 90° is fabricated by axial fabric (180 g/m^2 or 360 g/m^2) and the lamina with angle of ±45° is achieved by biaxial fabric (680 g/m^2).

2.2. Manufacture processing

As shown in Fig. 5, the pultrusion line [20] mainly includes: roving/fabric stacked on creels, pre-forming guide plate, resin impregnator, forming & curing die, pulling system and cutting system. Glass roving, axial fabric and biaxial fabric (in Fig. 6-a) are guided by pre-forming plate (in Fig. 6-b) from a creel into a resin impregnation tank (in Fig. 6-c) for wetting the reinforcements with polymeric matrix. The pre-forming plate guides positions of reinforcements at the designed locations in the cross section of profiles. The wetted reinforcements are then travels through heated die (in Fig. 6-d) to cure epoxy resin drawn by pulling system (in Fig. 6-e). The resin matrix progressively changes from liquid to gel and finally to solid. After performing and shaping, the composites are pulled out and cut off based on required length (in Fig. 6-f).

2.3. Lamina properties prediction

2.3.1. Fiber volume fractions and lamina thickness

The mechanical properties of E-glass fibers and epoxy resin are summarized in Tables 1 and 2 [21].

In the analysis, the reinforcement thickness of each lamina is defined as the product of the surface density of reinforcement and thickness constant while the resin thickness is assumed to be averagely distributed along the laminate thickness [16,17]. The predicted lamina's thickness and the fiber volume fractions based on material properties listed in Tables 1 and 2 are presented in Tables 3 and 4. The ratio of thickness of 0° lamina to total laminate is denoted as α, the ratio of thickness of 90° lamina to total laminate is denoted as β and the ratio of thickness of ±45° lamina to total laminate is denoted as γ.

2.3.2. Engineering constants

The engineering constants of each lamina include longitudinal modulus E_1, transverse modulus E_2, shear modulus G_{12}, and Poisson's ratio v_{12}, are approximated based on the modified role of mixture formulae [16,17]. The predicted lamina's engineering constants based on material properties listed in Tables 1 and 2 are presented in Table 5.

2.3.3. 3Ultimate strength

By assuming 1) the tensile strength of all fiber inclusions in composites have the same tensile or compressive strength, 2) the strength of unidirectional composite under longitudinal tension and compression are determined by the fibers and 3) the fibers are brittle compared with epoxy and behave linearly up to failure. The longitudinal tensile strength X_T and longitudinal compressive strength X_C may be predicted by Eqs. (1) and (2) [22] based on role of mixture:

$$X_T = X_{ft}(V_f + \frac{E_m}{E_{f1}} V_m) \quad (1)$$

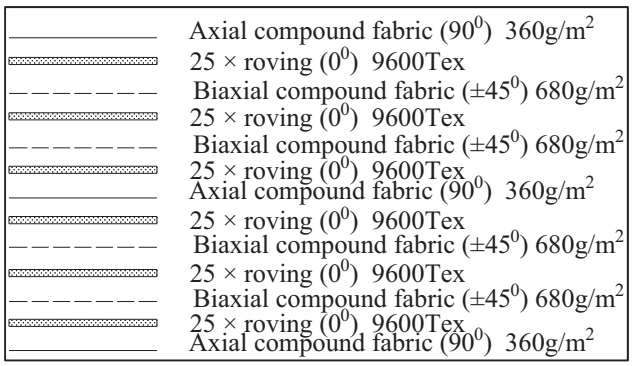

（a）GF600

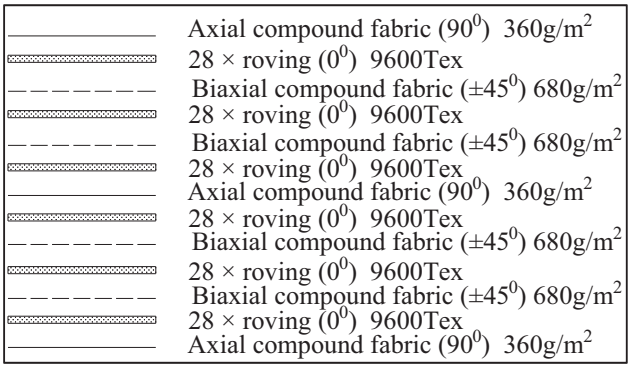

(b) GF700

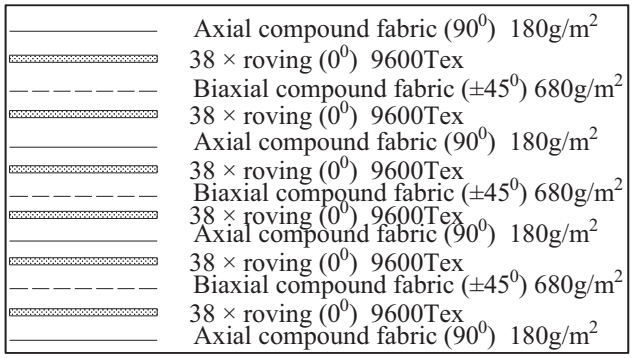

(c) GF800

Fig. 4. Laminate lay-up.

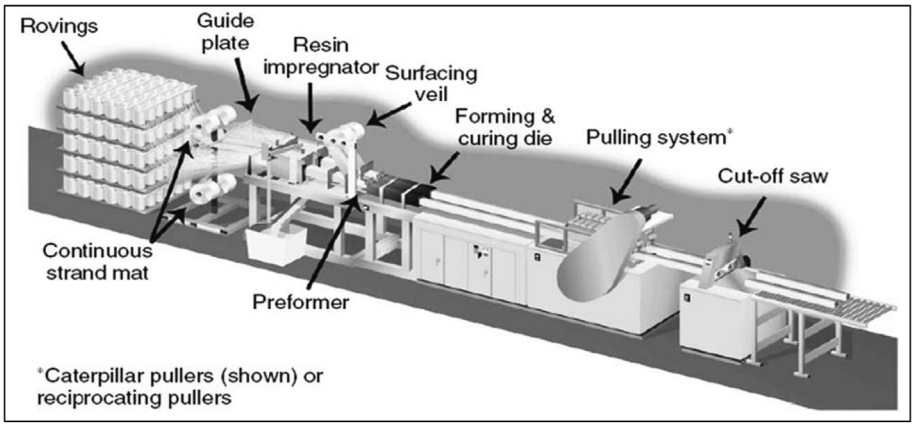

Fig. 5. Schematic of pultrusion process.

$$X_C = X_{fc}(V_f + \frac{E_m}{E_{f1}} V_m) \tag{2}$$

where X_{ft} is the tensile strength of fiber, X_{fc} is the compressive strength of fiber, V_f is the fiber volume fraction, V_m is the matrix volume fraction, E_{f1} is the longitudinal elastic modulus of fiber, E_m is the elastic modulus of matrix.

Due to stress concentrations by including fibers into matrix (resin), the transverse tensile strength of lamina caused by matrix failure is lower than the original tensile strength of the matrix. The transverse tensile strength of lamina Y_T is regarded as matrix tensile strength divided by stress concentration factor (SCF) adopted by Liu and Huang [23] as expressed in Eq. (3).

$$Y_T = \frac{X_{mt}}{\left[1 + \frac{\sqrt{V_f}}{2}\eta_1 + \frac{\sqrt{V_f}}{2}(3 - V_f - \sqrt{V_f})\eta_2\right]\left[\frac{(V_f+\beta V_m)E_{f2}+(1-\beta)V_m E_m}{\beta E_{f2}+(1-\beta)E_m}\right]} \tag{3}$$

where X_{mt} is the tensile strength of resin, E_{f2} is the transverse elastic modulus of fiber, η_1 and η_2 are constants as expressed in Eqs. (4) and (5), β is corrector coefficient and is assumed to be 0.7 in this paper.

$$\eta_1 = \frac{[1 - \upsilon_m - 2\upsilon_m^2]E_{f2} - [1 - \upsilon_f - 2\upsilon_f^2]E_m}{E_{f2}(1 + \upsilon_m) + E_m[1 - \upsilon_f - 2\upsilon_f^2]} \tag{4}$$

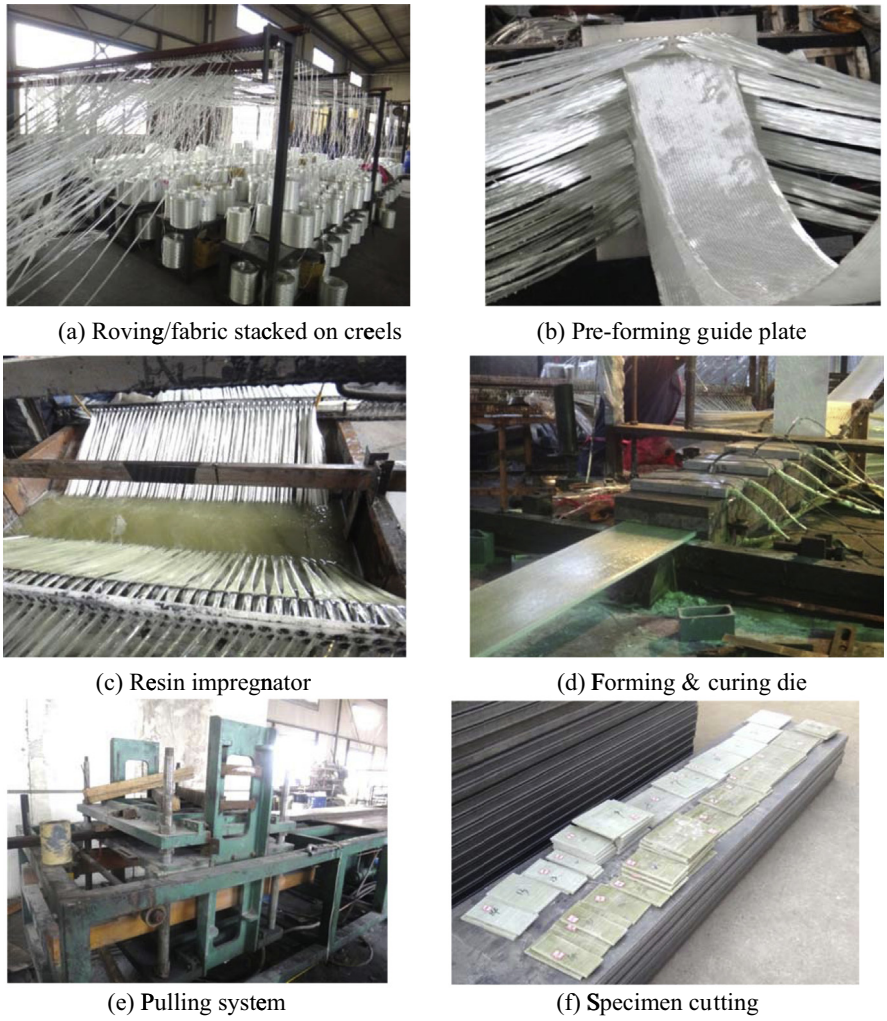

Fig. 6. Different stages of pultrusion process.

Table 1
Mechanical properties of E-glass fibers.

Longitudinal modulus (E_{f1})	Transverse modulus (E_{f2})	Poisson's ratio (v_f)	Shear modulus (G_f)	Tensile strength (X_{ft})	Compressive strength (X_{fc})	Density (ρ)
74.0 GPa	74.0 GPa	0.20	30.80 GPa	2150 MPa	1450 MPa	2560 kg/m^3

Table 2
Mechanical properties of epoxy resin.

Modulus (E_m)	Poisson's ratio (v_m)	Shear modulus (G_m)	Tensile strength (X_{mt})	Compressive strength (X_{mc})	Shear strength (S_m)	Density (ρ)
3.35 GPa	0.35	1.24 GPa	80 MPa	120 MPa	75 MPa	1,160 kg/m^3

$$\eta_2 = \frac{[1+v_f]E_m - [1+v_f]E_{f2}}{E_{f2}(-3+v_m+4v_m^2) - E_m[1+v_f]} \tag{5}$$

where v_m is the Possion's ratio of matrix, v_f is the Possion's ratio of fiber.

Without considering fracture mechanics, previous empirical formulas [22,24,25] were adopted to predict the transverse compression strength Y_C and in-plane shear strength S_L by Eqs. (6) and (7).

$$Y_C = Y_{mc}C_v\left[1+\left(V_f-\sqrt{V_f}\right)\left(1-\frac{E_m}{E_{f2}}\right)\right] \tag{6}$$

$$S_L = S_mC_v\left[1+\left(V_f-\sqrt{V_f}\right)\left(1-\frac{G_m}{G_f}\right)\right] \tag{7}$$

where C_v is empirical constant. It is assumed the C_v in transverse compression strength and in-plane shear strength is same. It could be calculated by Eq. (8). G_m is the shear modulus of the matrix, G_f is the shear modulus of fiber, Y_{mc} is the compression strength of matrix, S_m is the matrix shear strength..

$$C_v = 1-\sqrt{\frac{4V_v}{\pi(1-V_f)}} \tag{8}$$

where V_v is void volume fraction and is assumed to 0 in this paper.

The predicted lamina's ultimate strengths of each laminate were listed in the Table. 6. It is also noted that the strength of fabric layers were simply assumed as unidirectional roving layer with

Table 3
Lamina thickness of different pultruded laminate.

Number	reinforcement	GF800		GF700		GF600	
		Angle	Thickness/mm	Angle	Thickness/mm	Angle	Thickness/mm
Ply-1	fabric	90°	0.117	90°	0.274	90°	0.297
Ply-2	roving	0°	1.368	0°	1.184	0°	1.145
Ply-3	fabric	±45°	0.441	±45°	0.518	±45°	0.560
Ply-4	roving	0°	1.368	0°	1.184	0°	1.145
Ply-5	fabric	90°	0.117	±45°	0.518	±45°	0.560
Ply-6	roving	0°	1.368	0°	1.184	0°	1.145
Ply-7	fabric	±45°	0.441	90°	0.274	90°	0.297
Ply-8	roving	0°	1.368	0°	1.184	0°	1.145
Ply-9	fabric	90°	0.117	±45°	0.518	±45°	0.560
Ply-10	roving	0°	1.368	0°	1.184	0°	1.145
Ply-11	fabric	±45°	0.441	±45°	0.518	±45°	0.560
Ply-12	roving	0°	1.368	0°	1.184	0°	1.145
Ply-13	fabric	90°	0.117	90°	0.274	90°	0.297
Total thickness/mm		10		10		10	

Table 4
Fibers and matrix volume fraction.

	Fibers total	Matrix	α	β	γ
GF600	45.9%	44.1%	65.3%	11.5%	23.2%
GF700	50.5%	49.5%	67.8%	10.7%	21.5%
GF800	60.5%	39.5%	75.2%	11.6%	13.1%

Table 5
Lamina engineering constants of pultruded GFRP laminate.

Mechanical Properties	GF800	GF700	GF600
E_1 (GPa)	45.95	39.63	36.87
E_2 (GPa)	14.56	11.67	10.64
E_3 (GPa)	14.56	11.67	10.64
G_{12} (GPa)	4.50	3.59	3.27
G_{13} (GPa)	4.50	3.59	3.27
G_{23} (GPa)	5.51	4.34	3.93
v_{12}	0.25	0.27	0.28
v_{13}	0.25	0.27	0.28
v_{23}	0.30	0.32	0.33

Table 6
Lamina ultimate capacity of pultruded GFRP laminate.

Mechanical Properties	GF800	GF700	GF600
X_T (MPa)	1341.20	1158.90	988.80
Y_T (MPa)	47.80	48.90	49.60
Z_T (MPa)	47.80	48.90	49.60
X_C (MPa)	1048.40	908.20	837.70
Y_C (MPa)	100.10	96.90	95.30
Z_C (MPa)	100.10	96.90	95.30
S_{xy} (MPa)	65.50	64.80	64.90
S_{xz} (MPa)	65.50	64.80	64.90
S_{xz} (MPa)	65.50	64.80	64.90

special angles and the purpose of predicted strength is to provide initial reference in the finite element simulation.

3. Experimental programs and results

3.1. Material tests

The tensile and in-plane shear (45° off-axis tensile) of each laminate were experimentally evaluated in accordance to ISO 527[26] and ISO 14129 [27] standards, respectively. In consideration to the anisotropic nature and common scattered properties of commercially-produced pultruded composites, five specimens of each laminate were prepared and tested in both parallel- and perpendicular-to-fibers directions.

3.2. Experimental results

The average test value is denoted as X_{av}, the test value with 95% guaranteed rate is denoted as $X_{95\%}$, the design value suggested by Chinese Standard MOHURD GB50608-2010 [28] is denoted as X_k based on Eq. (9), the design value suggested by ASCE-MOP 102 [29] is denoted as X_{gr} based on Eq. (10), standard deviation is denoted as X_{SD}.

$$X_k = X_{av} - 1.645X_{SD} \tag{9}$$

$$X_{gr} = X_{av} - 3X_{SD} \tag{10}$$

The tensile results were summarized in Tables 7 and 8 with tensile strength denoted as T and with elastic module denoted as E. The Poisson's ratio results of each laminate are summarized in Table 9 with longitudinal Poisson's ratio denoted as v_{xy} and transverse Poisson's ratio denoted as v_{yx}. The in-plane shear results summarized in Table 10 with shear strength denoted as S and shear modulus denoted as G.

The failure modes of tensile specimens were shown in Fig. 7. The longitudinal tensile specimens (Fig. 7-a) presented transverse splitting in red rectangle and fracture near the clamped ends in red ellipse. The reason of splitting is that the deformation of each lamina is inconsistent while each lamina was bonded together. Inter-laminar stress was generated to consistent the deformation of each layer. Due to poor inter-laminar performance in such large thickness specimens, splitting occurred when the load increased to ultimate. The fracture near the clamped ends is mainly due to stress concentration caused by clamps. The transverse tensile specimens showed fracture appeared near the middle of the specimens, as depicted in Fig. 7-b. The reason is that the transverse fiber fraction is relatively low and all the laminas are snapped at the ultimate stage.

The failure modes of in-plane shear specimen are shown in Fig. 8. It presented fracture along fiber direction near the middle of the specimen. The reason is that the tensile load transferred to

Table 7
Summary of longitudinal tensile results.

Laminate lay-up	Longitudinal tensile strength/MPa						Longitudinal elastic modulus/GPa					
	T_{av}	T_{SD}	Number	$T_{95\%}$	T_k	T_{gr}	E_{av}	E_{SD}	Number	$E_{95\%}$	E_k	E_{gr}
GF600	682.3	6.60	5	674.15	671.44	662.5	28.70	0.94	5	27.66	27.33	26.21
GF700	786.43	3.98	5	781.49	779.88	774.49	35.95	1.22	5	34.44	33.94	32.29
GF800	838.39	5.10	5	832.06	830.00	823.09	42.39	1.17	5	40.94	40.47	38.88

Table 8
Summary of transverse tensile results.

Laminate lay-up	Transverse tensile strength/MPa						Transverse elastic modulus/GPa					
	T_{av}	T_{SD}	Number	$T_{95\%}$	T_k	T_{gr}	E_{av}	E_{SD}	Number	$E_{95\%}$	E_k	E_{gr}
GF600	138.73	4.95	5	132.58	130.59	123.88	16.90	1.09	5	15.52	15.11	13.63
GF700	131.85	2.74	5	128.45	127.34	123.63	16.60	0.77	5	15.64	15.33	14.29
GF800	86.42	2.15	5	83.75	82.88	79.97	17.12	0.55	5	16.43	16.21	15.47

Table 9
Summary of Poisson's ratio results.

Laminate lay-up	Longitudinal Poisson's ratio (v_{xy})			Transverse Poisson's ratio (v_{yx})		
	v_{xy}	$(v_{xy})_{SD}$	Number	v_{yx}	$(v_{yx})_{SD}$	Number
GF600	0.32	0.029	5	0.17	0.008	5
GF700	0.32	0.017	5	0.11	0.002	5
GF800	0.33	0.024	5	0.13	0.005	5

Table 10
Summary of in-plane shear results.

Laminate lay-up	In-plane shear strength/MPa						In-plane shear elastic modulus/GPa					
	S_{av}	S_{SD}	Number	$S_{95\%}$	S_k	S_{gr}	G_{av}	G_{SD}	Number	$G_{95\%}$	G_k	G_{gr}
GF600	86.87	7.54	5	77.49	74.47	64.25	5.78	0.27	5	5.45	5.34	4.97
GF700	79.12	7.29	5	70.07	67.13	57.25	6.06	0.19	5	5.82	5.75	5.49
GF800	76.06	2.48	5	72.99	71.98	68.62	6.34	0.17	5	6.13	6.06	5.83

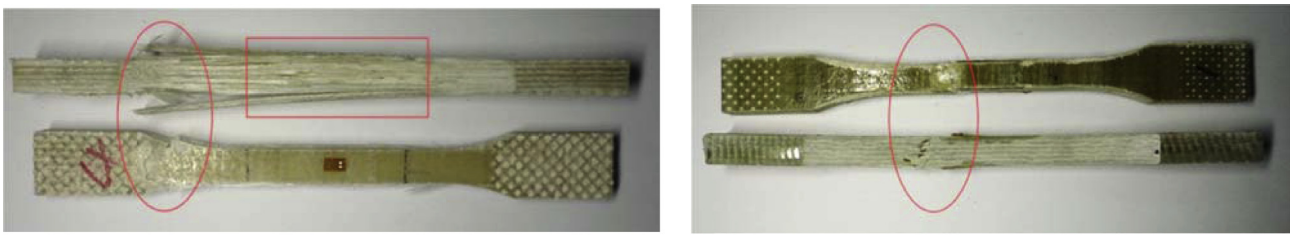

(a) Longitudinal (b) Transverse

Fig. 7. Failure mode of tensile specimen.

Fig. 8. Failure mode of in-plane shear specimen.

shear load due to angle (45°) between the fiber direction and perpendicular to fiber direction, the performance perpendicular to fiber direction is so weak compared with fiber direction that the specimen presented fracture along fiber direction.

3.3. Comparison between theoretical and experimental results

The comparison between theoretical results and test results is shown in Fig. 9. Detailed formulations and procedures to calculate the equivalent properties including the elastic modulus, the shear modulus and the Possion's ratio may refer to [16]. It is shown that the difference between all theoretical engineering constants and average test results is within 10%, indicating the theoretical results agreed well with test results. The difference of longitudinal elastic modulus and shear modulus between theoretical and suggested design value by MOHURD GB50608-2010 [28] is within 5%, while the difference between theoretical and suggested transverse elastic modulus by MOHURD GB50608-2010 [28] is 10%. The difference of longitudinal elastic modulus and shear modulus between theoretical and suggested design value by ASCE-MOP 102 [29] is almost 10%, while the transverse elastic modulus difference between theoretical and suggested design value by ASCE-MOP 102 [29] is almost 20%.

4. Carpet plots design

A laminate design consists of materials, number of lamina, lamina thickness and orientations and laminate stacking sequence. For the GFRP laminate in this study, the fiber is E-glass fiber and the resin is epoxy. The roving (0° lamina) is used to bear longitudinal load, the axial fabric (90° lamina) is used to bear transverse load and biaxial fabric (±45° lamina) is used to bear shear load. The in-plane engineering constants will not be influenced by laminate stacking sequence. Thus, fiber volume fraction, lamina thickness and orientations are the variation parameters of GFRP laminates' engineering constants.

The fiber volume fraction could vary over a broad range allowed by particular manufacturing process. Based on typical representative volume element (RVE) analysis, the possible maximum volume fraction of rectangular packing array is 78.5% [30]. Laminates' engineering constants variation with fiber fraction is shown in Fig. 10. The elastic modulus of GFRP laminates is between 4.2 GPa and 61 GPa, the shear modulus of GFRP laminates is between 1.57 GPa and 25.5 GPa and the Poisson's ratio of GFRP laminates is between 0.1 and 0.6.

Composites need to be stronger than the matrix, and practical composites should have minimum fiber fraction limit V_{min} based

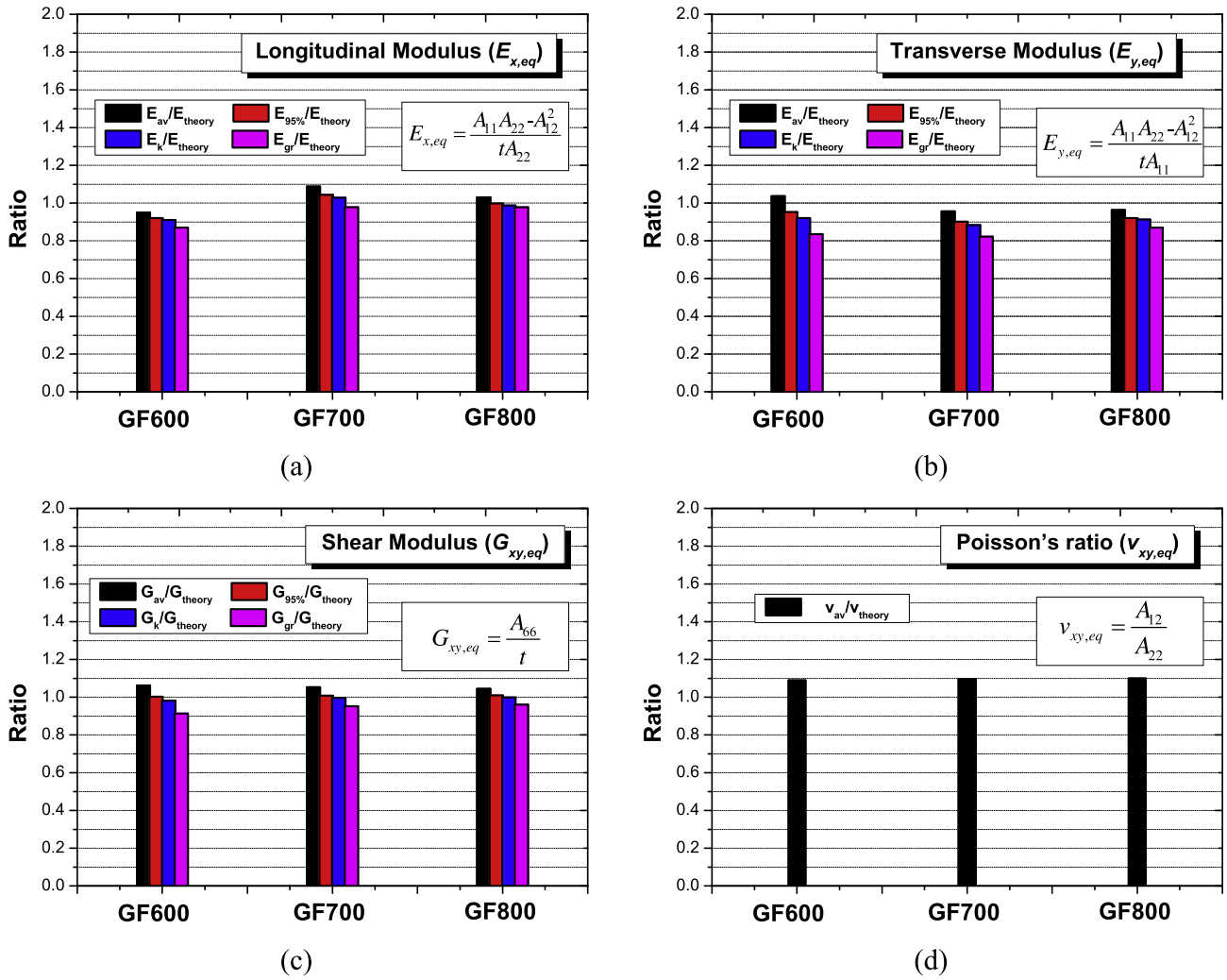

Fig. 9. Comparison of theoretical and test results.

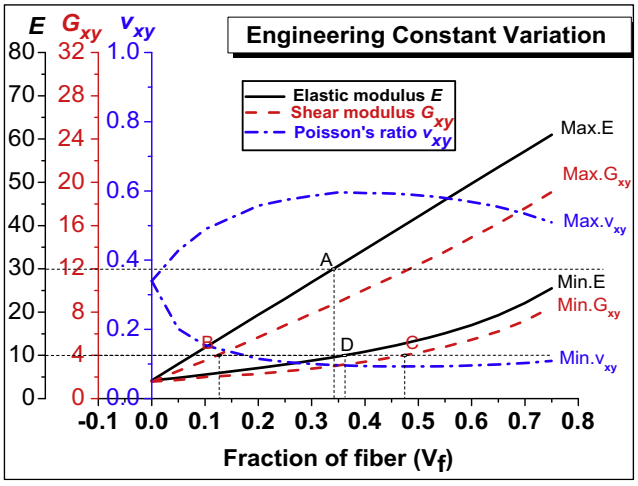

Fig. 10. Engineering constants variation along fiber fraction.

on Eq. (11). Besides, it is also need to consider minimum fiber fraction based on manufactory process [30]. The practical minimum fiber fraction is assumed to be 0.2 in this paper.

$$V_{\min} = \frac{E_{f1}X_{mt} - E_m X_{ft}}{E_{f1}X_{ft} - E_m X_{mt}} \tag{11}$$

where E_{f1} is longitudinal elastic modulus, X_{mt} is tensile strength of resin, E_m is elastic modulus of resin, X_{ft} is tensile strength of fiber.

Considering the facts that lack of knowledge of the majority of bridge engineers on the behavior of composites, a carpet plots with different fiber volume fraction are proposed to extend the laminate design procedure without much complicated calculations based on the micro-mechanics and macro-mechanics theoretical analysis. The carpet plots with fiber fraction from 20% to 75% is proposed in this paper, as is shown in Fig. 11 with ratio of thickness of ±45° lamina to total laminate as X-axis and elastic modulus, Poisson's ratio and shear modulus as Y-axis. The sum of ratio of α, β and γ is one. It is shown that the shear modulus increased linearly with ratio of thickness of ±45° lamina (γ) to total laminate increasing while elastic modulus and Poisson's ratio are non-uniform. The multi carpet plots allow designers to preliminary design and predict the engineering constants of GFRP laminate without calculation.

For example, if the designers want to design GFRP laminate with longitudinal elastic modulus (30 GPa), transverse elastic modulus (10.0 GPa) and shear modulus (4.0 GPa) based on practical requirements, it is needed to confirm fiber fraction and ratio of lamina thickness to total laminates. Due to the maximum elastic modulus is in the case that all the lamina is along the fiber direction while the minimum elastic modulus is in the case that all the lamina is along the perpendicular to the fiber direction. Thus, the designed value of longitudinal elastic modulus should be larger than the maximum elastic modulus and the designed value of transverse elastic modulus should be larger than minimum elastic modulus. According to Fig. 10, the required longitudinal elastic modulus (Point "A" in Fig. 10) suggested the fiber fraction should be larger than 0.35. The required shear modulus (Points "B" and "C" in Fig. 10) suggested the fiber fraction should be between 0.15 and 0.50. The required transverse elastic modulus (Point "D" in Fig. 10) suggested the fiber fraction should be larger than 0.36. Thus, the fiber fraction is determined between 0.40 and 0.50 in the innovative multi carpet plots by considering longitudinal and transverse elastic modulus and shear modulus.

We start the design with carpet plots with fiber fraction 0.4. We firstly confirm the ±45° lamina fraction is 0.10 (Point "A" in Fig. 11-h) based on the in-plane shear modulus design value (4.0 GPa), and confirm the 0° lamina fraction is 0.80 (Point "B" in Fig. 11-h) based on the longitudinal elastic modulus design value (30.0 GPa). Thus, the 90° lamina fraction is 0.1 based on the sum of three fractions is one. One can estimate the transverse elastic modulus with the 90° lamina fraction of as 13.75 GPa (Point "C" in Fig. 11-h) that meet the transverse elastic modulus requirement 10.0 GPa. The Poisson's ratio of this laminate could also be estimated to be between 0.24 and 0.25 (Point "D" in Fig. 11-h). Finally, the fiber volume fraction is suggested as 40%, α is suggested as 0.8, β is suggested as 0.1 and γ is suggested as 0.1.

5. Continuum damage model and program implementation

Continuum damage material model of PFRP was implemented based on the User-material subroutine UMAT in ABAQUS/Standard [31].

5.1. Damaged material response

In terms of continuum damage mechanics, the effective stress $\bar{\sigma}$ and the nominal stress, σ, is postulated to have the following form [32]:

$$\bar{\sigma}_{ij} = M_{ijkl}(d_i)\sigma_{kl} \tag{12}$$

where M_{ijkl} is fourth order damage operator which has the diagonal form. d_i is damage variable. For three dimensional laminas, the following form of damage operator M_{ijkl} [33] is adopted in this paper: where: d_f, d_m and d_d are damage variables for fiber failure, matrix failure in transverse direction and matrix failure in thickness direction respectively.

$$M = \begin{bmatrix} \frac{1}{\sqrt{1-d_f}} & 0 & 0 & 0 & 0 & 0 \\ & \frac{1}{\sqrt{1-d_m}} & 0 & 0 & 0 & 0 \\ & & \frac{1}{\sqrt{1-d_d}} & 0 & 0 & 0 \\ & & & \frac{1}{\sqrt{(1-d_f)(1-d_m)}} & 0 & 0 \\ & \textit{Symmetric} & & & \frac{1}{\sqrt{(1-d_f)(1-d_d)}} & 0 \\ & & & & & \frac{1}{\sqrt{(1-d_m)(1-d_d)}} \end{bmatrix} \tag{13}$$

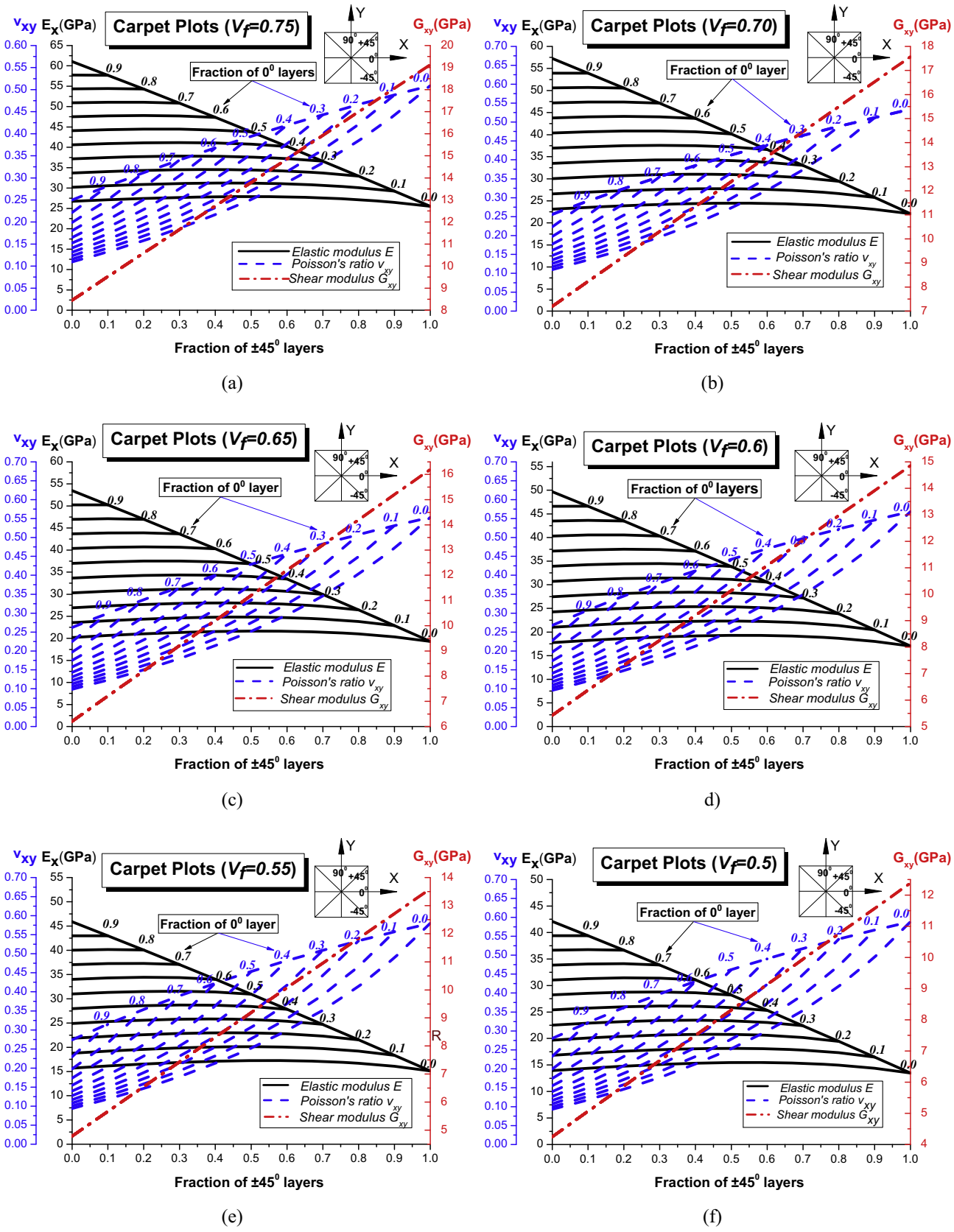

Fig. 11. Carpet plots with different fiber fraction.

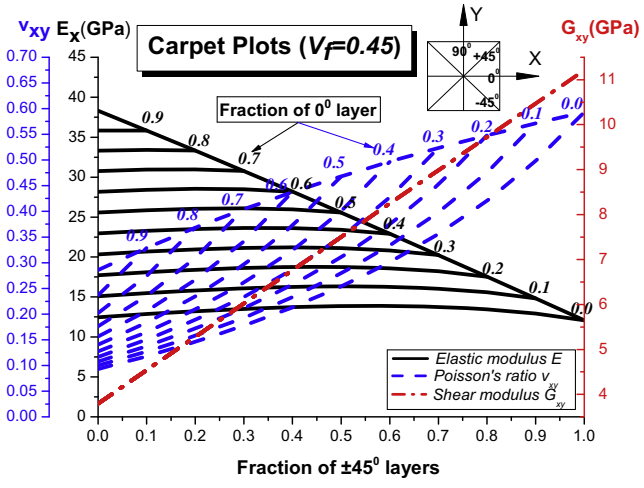

(g)

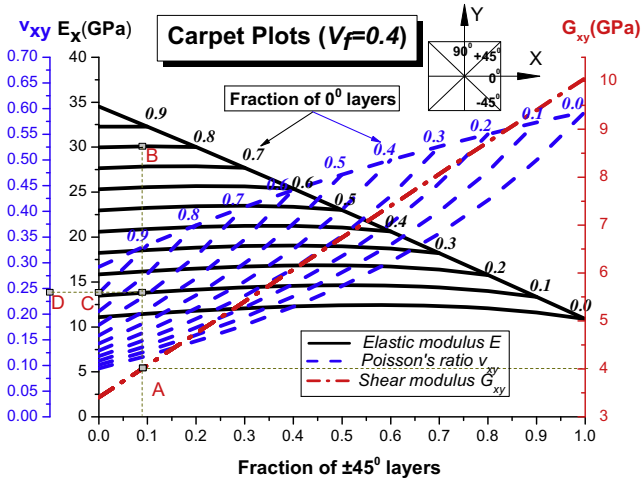

(h)

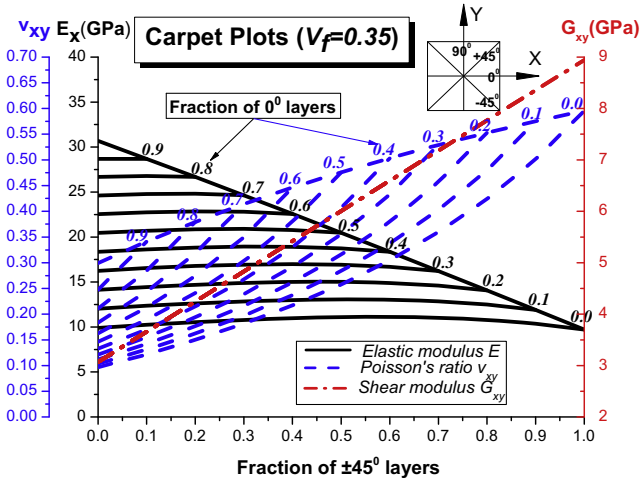

(i)

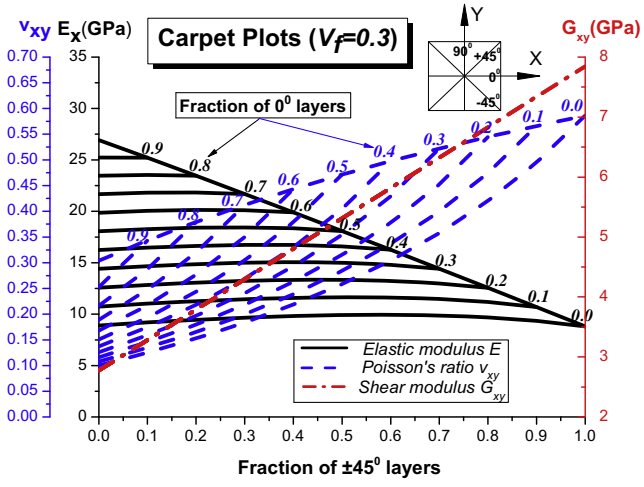

(g)

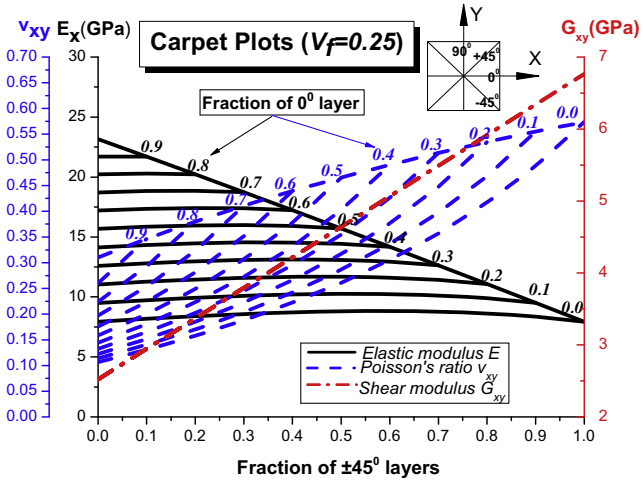

(h)

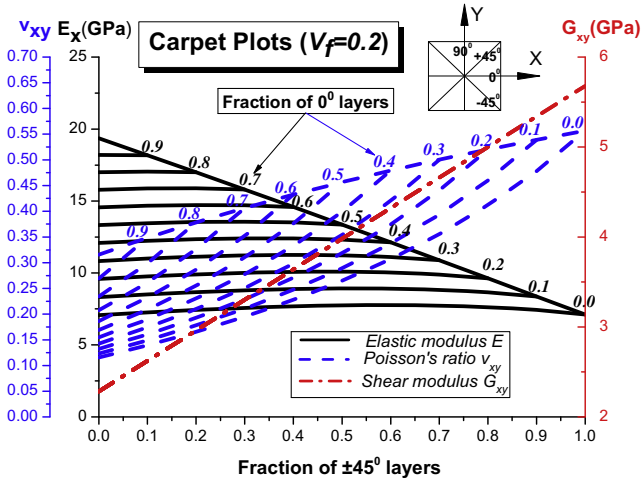

(k)

Fig. 11 (*continued*)

The elastic constitutive relationship is adopted as following:

$$\sigma_{ij} = C_{ijkl}\varepsilon_{kl} \tag{14}$$

where: C_{ijkl} is damage-free stiffness matrix, and Eq. (14) is expressed as follows:

$$\begin{bmatrix}\sigma_{11}\\ \sigma_{22}\\ \sigma_{33}\\ \sigma_{12}\\ \sigma_{13}\\ \sigma_{23}\end{bmatrix} = \begin{bmatrix} \frac{1-\nu_{23}\nu_{32}}{E_2E_3\Delta} & \frac{\nu_{21}+\nu_{31}\nu_{23}}{E_2E_3\Delta} & \frac{\nu_{31}+\nu_{21}\nu_{32}}{E_2E_3\Delta} & 0 & 0 & 0 \\ & \frac{1-\nu_{31}\nu_{13}}{E_1E_3\Delta} & \frac{\nu_{32}+\nu_{31}\nu_{12}}{E_1E_3\Delta} & 0 & 0 & 0 \\ & & \frac{1-\nu_{21}\nu_{12}}{E_1E_2\Delta} & 0 & 0 & 0 \\ & \textit{Symmetric} & & G_{12}+f(\gamma_{12}) & 0 & 0 \\ & & & & G_{13}+f(\gamma_{13}) & 0 \\ & & & & & G_{23}+f(\gamma_{23}) \end{bmatrix} \begin{bmatrix}\varepsilon_{11}\\ \varepsilon_{22}\\ \varepsilon_{33}\\ \gamma_{12}\\ \gamma_{13}\\ \gamma_{23}\end{bmatrix} \tag{15}$$

$$\frac{\nu_{ij}}{E_i} = \frac{\nu_{ji}}{E_j} \quad i,j = 1,2,3 \tag{16}$$

$$\Delta = \frac{1-\nu_{12}\nu_{21}-\nu_{23}\nu_{32}-\nu_{31}\nu_{13}-2\nu_{21}\nu_{32}\nu_{12}}{E_1E_2E_3} \tag{17}$$

where: E_1, E_2 and E_3 are the lamina longitudinal moduli, G_{12}, G_{13} and G_{23} are the shear moduli, ν_{12}, ν_{13} and ν_{23} are the Poisson's ratio. The extra term f of shear modulus in the damage-free stiffness matrix is used to describe the non-linear shear behavior of each lamina [34] as below:

$$\gamma_{ij} = \frac{1}{G_{ij}}\sigma_{ij} + \alpha_k(\sigma_{ij})^3 \quad i \neq j \tag{18}$$

where: α_k (k = 1,2,3) is nonnegative material parameter to describe nonlinear of the in-plane shear behavior. α_1 is used to describe the shear nonlinear along 1–2 direction, α_2 is used to describe the shear nonlinear along 1–3 direction, and α_3 is used to describe the shear nonlinear along 2–3 direction. Above equation could further expressed as [34]:

$$\sigma_{ij} = [G_{ij} + f(\gamma_{ij})]\gamma_{ij} \quad i = 1, j = 2,3 \tag{19}$$

where: $f(\gamma_{ij})$ is the real root of the equation which could be solved by Eqs. (20)–(22).

$$y^3 + 3G_{ij}y^2 + \left(3G_{ij}^2 + \frac{G_{ij}}{\alpha}\frac{1}{\gamma_{ij}}\right)y + G_{ij}^3 = 0 \quad i = 1, j = 2,3 \tag{20}$$

$$f(\gamma_{ij}) = -\frac{b}{3a} + \sqrt[3]{\frac{bc}{6a^2} - \frac{b^3}{27a^3} - \frac{d}{2a} + \sqrt{\left(\frac{bc}{6a^2} - \frac{b^3}{27a^3} - \frac{d}{2a}\right)^2 + \left(\frac{c}{3a} - \frac{b^2}{9a^2}\right)^3}} + \sqrt[3]{\frac{bc}{6a^2} - \frac{b^3}{27a^3} - \frac{d}{2a} - \sqrt{\left(\frac{bc}{6a^2} - \frac{b^3}{27a^3} - \frac{d}{2a}\right)^2 + \left(\frac{c}{3a} - \frac{b^2}{9a^2}\right)^3}} \tag{21}$$

$$a = 1, b = 3G_{ij}, c = 3G_{ij}^2 + \frac{G_{ij}}{\alpha_k}\frac{1}{\gamma_{ij}}, d = G_{ij}^3 \quad i = 1, j = 2,3 \tag{22}$$

To obtain damage-dependent material property, effective stiffness matrix is introduced and denoted as $\bar{C}_{ijkl}$. By employing the postulate of complementary elastic energy equivalence between $\bar{\sigma}$ and σ [33,35]:

$$\sigma_{ij}\bar{C}_{ijkl}\sigma_{kl} = \bar{\sigma}_{ij}C_{ijkl}\bar{\sigma}_{kl} \tag{23}$$

which yields:

$$\bar{\sigma}_{ij} = \bar{C}_{ijkl}\varepsilon_{kl} \tag{24}$$

$$\bar{C}_{ijkl} = M_{ijkl}^{-1}C_{ijkl}M_{ijkl}^{-T} \tag{25}$$

5.2. Initial failure criteria

The modified Hashin's theory [36,37] was employed as initiation failure criteria to consider the lamina damage/failure along the thickness direction:

Fiber tensile damage ($\sigma_{11} > 0$):

$$F_{ft} = \Psi_{ft}(\sigma_{ij}) = \left(\frac{\sigma_{11}}{X^T}\right)^2 \geqslant 1 \tag{26}$$

Fiber compressive damage ($\sigma_{11} < 0$):

$$F_{fc} = \Psi_{fc}(\sigma_{ij}) = \left(\frac{\sigma_{11}}{X^C}\right)^2 \geqslant 1 \tag{27}$$

Matrix tensile damage in transverse direction ($\sigma_{22} > 0$):

$$F_{mt} = \Psi_{mt}(\sigma_{ij}) = \left(\frac{\sigma_{22}}{Y^T}\right)^2 + \left(\frac{\sigma_{12}}{S_{xy}}\right)^2 + \left(\frac{\sigma_{23}}{S_{yz}}\right)^2 \geqslant 1 \tag{28}$$

Matrix compressive damage in transverse direction ($\sigma_{22} < 0$):

$$F_{mc} = \Psi_{mc}(\sigma_{ij}) = \left(\frac{\sigma_{22}}{Y^C}\right)^2 + \left(\frac{\sigma_{12}}{S_{xy}}\right)^2 + \left(\frac{\sigma_{23}}{S_{yz}}\right)^2 \geqslant 1 \tag{29}$$

Matrix tensile damage in thickness direction ($\sigma_{33} > 0$):

$$F_{dt} = \Psi_{dt}(\sigma_{ij}) = \left(\frac{\sigma_{33}}{Z^t}\right)^2 + \left(\frac{\sigma_{12}}{S_{xy}}\right)^2 + \left(\frac{\sigma_{23}}{S_{yz}}\right)^2 \geqslant 1 \tag{30}$$

Matrix compressive damage in thickness direction ($\sigma_{33} > 0$):

$$F_{dc} = \Psi_{dc}(\sigma_{ij}) = \left(\frac{\sigma_{33}}{Z^c}\right)^2 + \left(\frac{\sigma_{12}}{S_{xy}}\right)^2 + \left(\frac{\sigma_{23}}{S_{yz}}\right)^2 \geqslant 1 \tag{31}$$

5.3. Damage assesment

Once a damage initiation is detected, further loading will cause degradation of material stiffness. The reduction of the stiffness coefficients depended on damage variables that are assumed between zero (damage initiation) and one (fully damage). The evolution of each damage variable is assumed to be governed by equivalent displacement. As is shown in Figs. 12 and 13, the damage variable of each failure mode i is given as following relationship [38]:

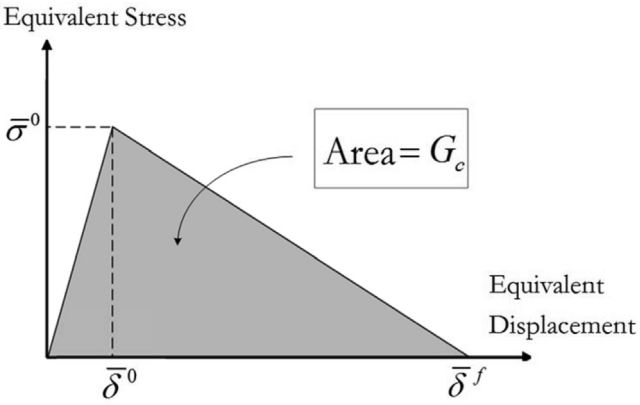

Fig. 12. Equivalent stress and equivalent displacement.

$$d_i = G(d_i) = \begin{cases} 0 & \bar{\delta}_i \leqslant \bar{\delta}_i^0 \\ \frac{\bar{\delta}_i^f(\bar{\delta}_i - \bar{\delta}_i^0)}{\bar{\delta}_i(\bar{\delta}_i^f - \bar{\delta}_i^0)} & \bar{\delta}_i^0 < \bar{\delta} \leqslant \bar{\delta}_i^f \quad i = f, m, d \\ d_{\max} & \bar{\delta} > \bar{\delta}_i^f \end{cases} \tag{32}$$

where the failure modes f, m and d failure modes indicate the fiber damage, matrix damage along the transverse direction and matrix damage along the thickness direction.

As is shown in Fig. 14, the initial damaged equivalent displacement/stress is assumed to be the intersection point of equivalent displacement/stress and yield surface. If one regards the equivalent displacement/stress as a line with certain loading direction, the angle φ between the loading direction line and "r_2-r_3" plane could be obtained by Eq. (33), and the angle θ between the projections in "r_2-r_3" plane of the loading direction line and axis "r_2" could be acquired by Eq. (34).

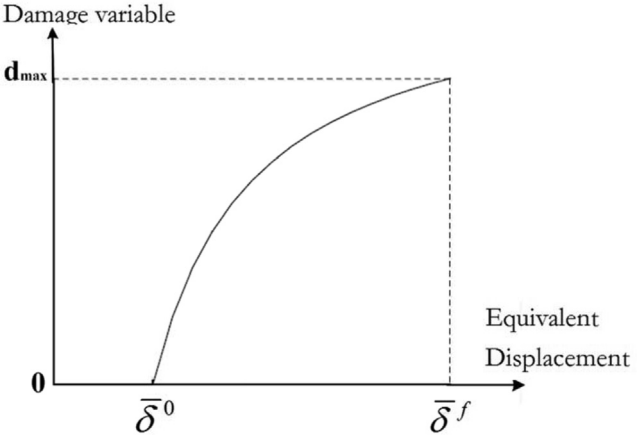

Fig. 13. Damage variable and equivalent displacement.

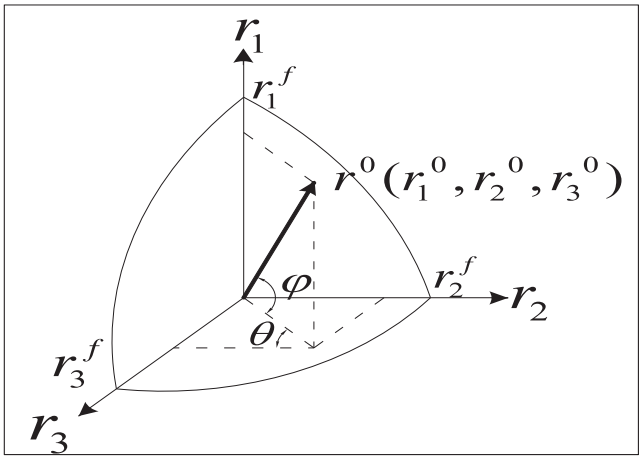

Fig. 14. Damage surface and equivalent displacement.

$$\varphi = \arcsin\left(\frac{r_1}{r}\right) = \arcsin\left(\frac{r_1}{\sqrt{r_1^2 + r_2^2 + r_3^2}}\right) \tag{33}$$

$$\theta = \arcsin\left(\frac{r_3}{\sqrt{r_2^2 + r_3^2}}\right) \tag{34}$$

Thus, the equivalent displacement/strain could be expressed as following:

$$r_1 = r\sin(\varphi), r_2 = r\cos(\varphi)\cos(\theta), r_3 = r\cos(\varphi)\sin(\theta) \tag{35}$$

Based on the general yield surfaces expression in Eq. (36), the intersection point is in both the yield surface and the loading direction, which could be expressed as Eq. (37).

$$\left(\frac{r_1}{r_1^f}\right)^2 + \left(\frac{r_2}{r_2^f}\right)^2 + \left(\frac{r_3}{r_3^f}\right)^2 = 1 \tag{36}$$

$$\left(\frac{r^0\sin(\varphi)}{r_1^f}\right)^2 + \left(\frac{r^0\cos(\varphi)\cos(\theta)}{r_2^f}\right)^2 + \left(\frac{r^0\cos(\varphi)\sin(\theta)}{r_3^f}\right)^2 = 1 \tag{37}$$

which yields,

$$r^0 = 1/\sqrt{\left(\frac{\sin(\varphi)}{r_1^f}\right)^2 + \left(\frac{\cos(\varphi)\cos(\theta)}{r_2^f}\right)^2 + \left(\frac{\cos(\varphi)\sin(\theta)}{r_3^f}\right)^2} \tag{38}$$

The initial damage equivalent displacement and initial damage equivalent stress could be obtained based on above equations. The details of initial damage equivalent displacement and initial damage equivalent stress of each failure modes is listed in Table. 11. The fully damage equivalent displacement is expressed as follows:

$$\delta_{eq,i}^f = \frac{2G_{i,c}}{\sigma_{i,eq}} \quad i = ft, fc, mt, mc, dt, dc \tag{39}$$

where $G_{i,c}$ is the fracture energy of each failure mode.

5.4. Loading/Unloading

The loading functions obey the loading–unloading conditions in the Kuhn-Tucker conditions [39], written as:

$$\dot{\delta}_{eq,i}^0 \geqslant 0, \quad f(\delta_{eq,i}, \delta_{eq,i}^0) \leqslant 0, \quad \dot{\delta}_{eq,i} f(\delta_{eq,i}, \delta_{eq,i}^0) = 0 \tag{40}$$

$$\dot{\delta}_{eq,i} \dot{f}(\delta_{eq,i}, \delta_{eq,i}^0) = 0 \quad (f(\delta_{eq,i}, \delta_{eq,i}^0) = 0) \tag{41}$$

5.5. Viscous regularization

Materials models with softening behavior and stiffness degradation generally have convergence difficulties in implicit finite element method. In order to alleviate convergence difficulties, a viscous regularization scheme is adopted [40] and a viscous damage variable is defined by the evolution equations:

$$\dot{d}_i^v = \frac{1}{\eta_i}(d_i - d_i^v) \tag{42}$$

Table 11
Details of equivalent displacement/stress.

Failure mode	Equivalent displacement δ_{eq}	Initial damage equivalent displacement δ^0_{eq}	Initial damage equivalent stress σ^0_{eq}	$\sin(\varphi)^2$	$\sin(\theta)^2$
Fiber tensile damage	$l_c\varepsilon_{11}$	$l_c\varepsilon^{f,t}_{11}$	X^T	–	–
Fiber compressive damage	$l_c\langle\varepsilon_{11}\rangle$	$l_c\varepsilon^{f,c}_{11}$	X^C	–	–
Matrix tensile damage in transverse direction	$l_c\sqrt{\varepsilon^2_{22}+\varepsilon^2_{12}+\varepsilon^2_{23}}$	$\frac{l_c}{\sqrt{(\frac{\sin(\varphi)}{\varepsilon^{f,t}_{22}})^2+(\frac{\cos(\varphi)\cos(\theta)}{\varepsilon^f_{12}})^2+(\frac{\cos(\varphi)\sin(\theta)}{\varepsilon^f_{23}})^2}}$	$\frac{1}{\sqrt{(\frac{\sin(\varphi)}{Y^T})^2+(\frac{\cos(\varphi)\cos(\theta)}{S_{12}})^2+(\frac{\cos(\varphi)\sin(\theta)}{S_{23}})^2}}$	$\frac{\varepsilon^2_{22}}{\sqrt{\varepsilon^2_{22}+\varepsilon^2_{12}+\varepsilon^2_{23}}}$	$\frac{\varepsilon^2_{23}}{\sqrt{\varepsilon^2_{12}+\varepsilon^2_{23}}}$
Matrix compressive damage in transverse direction	$l_c\sqrt{\varepsilon^2_{22}+\varepsilon^2_{12}+\varepsilon^2_{23}}$	$\frac{l_c}{\sqrt{(\frac{\sin(\varphi)}{\varepsilon^{f,c}_{22}})^2+(\frac{\cos(\varphi)\cos(\theta)}{\varepsilon^f_{12}})^2+(\frac{\cos(\varphi)\sin(\theta)}{\varepsilon^f_{23}})^2}}$	$\frac{1}{\sqrt{(\frac{\sin(\varphi)}{Y^C})^2+(\frac{\cos(\varphi)\cos(\theta)}{S_{12}})^2+(\frac{\cos(\varphi)\sin(\theta)}{S_{23}})^2}}$	$\frac{\varepsilon^2_{22}}{\sqrt{\varepsilon^2_{22}+\varepsilon^2_{12}+\varepsilon^2_{23}}}$	$\frac{\varepsilon^2_{23}}{\sqrt{\varepsilon^2_{12}+\varepsilon^2_{23}}}$
Matrix tensile damage in thickness direction	$l_c\sqrt{\varepsilon^2_{33}+\varepsilon^2_{13}+\varepsilon^2_{23}}$	$\frac{l_c}{\sqrt{(\frac{\sin(\varphi)}{\varepsilon^{f,t}_{33}})^2+(\frac{\cos(\varphi)\cos(\theta)}{\varepsilon^f_{13}})^2+(\frac{\cos(\varphi)\sin(\theta)}{\varepsilon^f_{23}})^2}}$	$\frac{1}{\sqrt{(\frac{\sin(\varphi)}{Z^T})^2+(\frac{\cos(\varphi)\cos(\theta)}{S_{13}})^2+(\frac{\cos(\varphi)\sin(\theta)}{S_{23}})^2}}$	$\frac{\varepsilon^2_{33}}{\sqrt{\varepsilon^2_{33}+\varepsilon^2_{13}+\varepsilon^2_{23}}}$	$\frac{\varepsilon^2_{23}}{\sqrt{\varepsilon^2_{13}+\varepsilon^2_{23}}}$
Matrix compressive damage in thickness direction	$l_c\sqrt{\varepsilon^2_{33}+\varepsilon^2_{13}+\varepsilon^2_{23}}$	$\frac{l_c}{\sqrt{(\frac{\sin(\varphi)}{\varepsilon^{f,c}_{33}})^2+(\frac{\cos(\varphi)\cos(\theta)}{\varepsilon^f_{13}})^2+(\frac{\cos(\varphi)\sin(\theta)}{\varepsilon^f_{23}})^2}}$	$\frac{1}{\sqrt{(\frac{\sin(\varphi)}{Z^C})^2+(\frac{\cos(\varphi)\cos(\theta)}{S_{13}})^2+(\frac{\cos(\varphi)\sin(\theta)}{S_{23}})^2}}$	$\frac{\varepsilon^2_{33}}{\sqrt{\varepsilon^2_{33}+\varepsilon^2_{13}+\varepsilon^2_{23}}}$	$\frac{\varepsilon^2_{23}}{\sqrt{\varepsilon^2_{13}+\varepsilon^2_{23}}}$

Note: l_c is characteristic length of the element. $\varepsilon^{f,t}_{11}=\frac{X^T}{E_1}$, $\varepsilon^{f,c}_{11}=\frac{X^C}{E_1}$, $\varepsilon^{f,t}_{22}=\frac{Y^T}{E_2}$, $\varepsilon^{f,c}_{22}=\frac{Y^C}{E_2}$, $\varepsilon^{f,t}_{33}=\frac{Z^T}{E_3}$, $\varepsilon^{f,C}_{33}=\frac{Z^C}{E_3}$, $\varepsilon^f_{12}=\frac{S_{12}}{G_{12}}$, $\varepsilon^f_{13}=\frac{S_{13}}{G_{13}}$, $\varepsilon^f_{23}=\frac{S_{23}}{G_{23}}$.

where η_l is a viscosity coefficient representing the relaxation time of the viscous system and d^v_l denotes regularized damage variable for mode *I*.

5.6. Implementation

The finite element equations by discretizing the virtual work equations are generally nonlinear, and the Newton–Raphson technique is used to solve the resulting system of nonlinear equations in ABAQUS [31]. It is important that the material tangent constitutive tensor is computed correctly to ensure robustness of the Newton–Raphson method. It is computed from the following equation:

$$\frac{\partial\sigma}{\partial\varepsilon}=\bar{C}+\sum_i\frac{\partial\bar{C}}{\partial d^v_i}\frac{\partial d^v_i}{\partial d_i}\frac{\partial d_i}{\partial\bar{\varepsilon}_i}\frac{\partial\bar{\varepsilon}_i}{\partial\varepsilon_i} \tag{43}$$

The detailed implementation algorithm is summarized in Box. 1.

Box 1: Implementation algorithm

1 Initial variable: $\{{}^nd_i, {}^nd^v_i, {}^nr_i, {}^nF_i\}\ i=f,m,d$
2 Update strain: ${}^{n+1}\varepsilon_i={}^n\varepsilon_i+\Delta\varepsilon_i\ i=1\ldots6$
3 Judge initial failure: ${}^{n+1}F_i=\max[\psi(\sigma_{ij}),{}^nF_i]i=f,m,d$
4 Update stress and Jacobian Matrix:
4-1 If ${}^{n+1}F_f<1$ &
${}^{n+1}F_m<1\&{}^{n+1}F_d<1{}^{n+1}\sigma_{ij}=C_{ijkl}{}^{n+1}\varepsilon_{kl}{}^{n+1}(\frac{\partial\sigma_{ij}}{\partial\bar{\varepsilon}_{kl}})=C_{ijkl}$
4-2 Else $(i=f,m,d)$:
4-2-1: compute ${}^{n+1}\delta_{eq,i}$
4-2-2: ① if ${}^{n+1}\delta_{eq,i}\leqslant{}^nr_i$:
${}^{n+1}r_i={}^nr_i$
${}^{n+1}d_i={}^nd_i$
${}^{n+1}d^v_i={}^nd^v_i$
② if ${}^{n+1}\delta_{eq,i}>{}^nr_i$:
${}^{n+1}r_i={}^{n+1}\delta_{eq,i}$
Compute ${}^{n+1}\delta^0_{eq,i}$, ${}^{n+1}\sigma^f_{eq,i}$, ${}^{n+1}\delta^f_{eq,i}$,
${}^{n+1}d_i=G({}^{n+1}\delta_{eq,i})$
${}^{n+1}d^v_i=\frac{\eta_i}{\eta_i+\Delta t}{}^nd^v_i+\frac{\Delta t}{\eta_i+\Delta t}{}^{n+1}d_i$
4-2-3: calculate equivalent stiffness:
${}^{n+1}\bar{C}_{mnkl}=M^{-1}_{mnkl}({}^{n+1}d^v_i)C_{mnkl}M^{-T}_{mnkl}({}^{n+1}d^v_i)$
4-2-4: Update stress: ${}^{n+1}\sigma_{mn}={}^{n+1}\bar{C}_{mnkl1}{}^{n+1}\varepsilon_{kl}$
4-2-5: Update Jacobian Matrix:
$n+1(\frac{\partial\sigma}{\partial\varepsilon})={}^{n+1}\bar{C}+\sum_i\frac{\partial^{n+1}\bar{C}}{\partial^{n+1}d^v_i}\frac{\partial^{n+1}d^v_i}{\partial^{n+1}d_i}\frac{\partial^{n+1}d_i}{\partial^{n+1}\bar{\varepsilon}_i}\frac{\partial^{n+1}\bar{\varepsilon}_i}{\partial^{n+1}\varepsilon_i}$

Table 12
Fracture energies of fiber-reinforced epoxy.

$G_{ft,c}$ (N/mm)	$G_{fc,c}$ (N/mm)	$G_{mt,c}$ (N/mm)	$G_{mc,c}$ (N/mm)
12.5	12.5	5.0	5.0

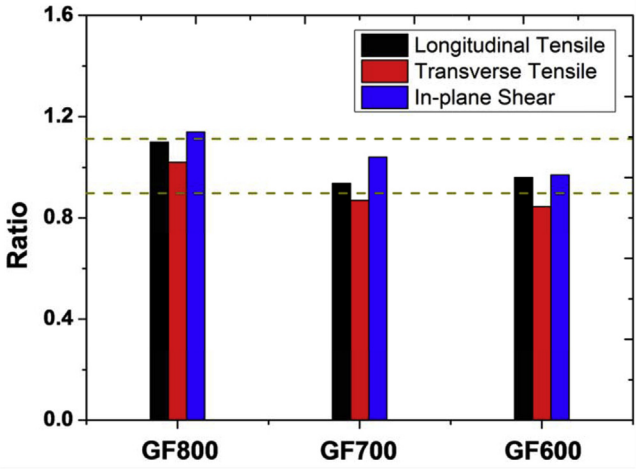

Fig. 15. Comparison between numerical and experimental ultimate capacities.

5.7. Numerical simulation description & results

The behaviors of each laminates were simulated numerically using the commercial finite element software ABAQUS/Standard. Each lamina was simulated by solid element C3D8R with enhanced hourglass stiffness control strategy based on the thickness information in Table 3. It should be noted that the stitched fabric layers, was regarded as unidirectional layers with special angles. The engineering constants of each PFRP lamine used in the simulation model were listed in Table 5. The in-plane shear nonlinear parameters α_1 and α_2 is assumed to be $7.20\times10^{-9}\,\mathrm{MPa}^{-3}$ based on Ref. [34] while the transverse shear nonlinear parameters α_3 is assumed to be zero. The initiation damage properties of PFRP lamina were assumed same and listed in Table 8. The viscosity coefficient of fiber failure mode is assumed to be 0.001 s while the viscosity coefficient of matrix failure mode 0.01 s considering the

matrix always reached damage status firstly. The values of fracture energy used in this paper are listed in Table 12 based on numerical tests. It is noted that the fracture energy is much higher than that used in the Refs. [16,17] and experimental fracture energy may be

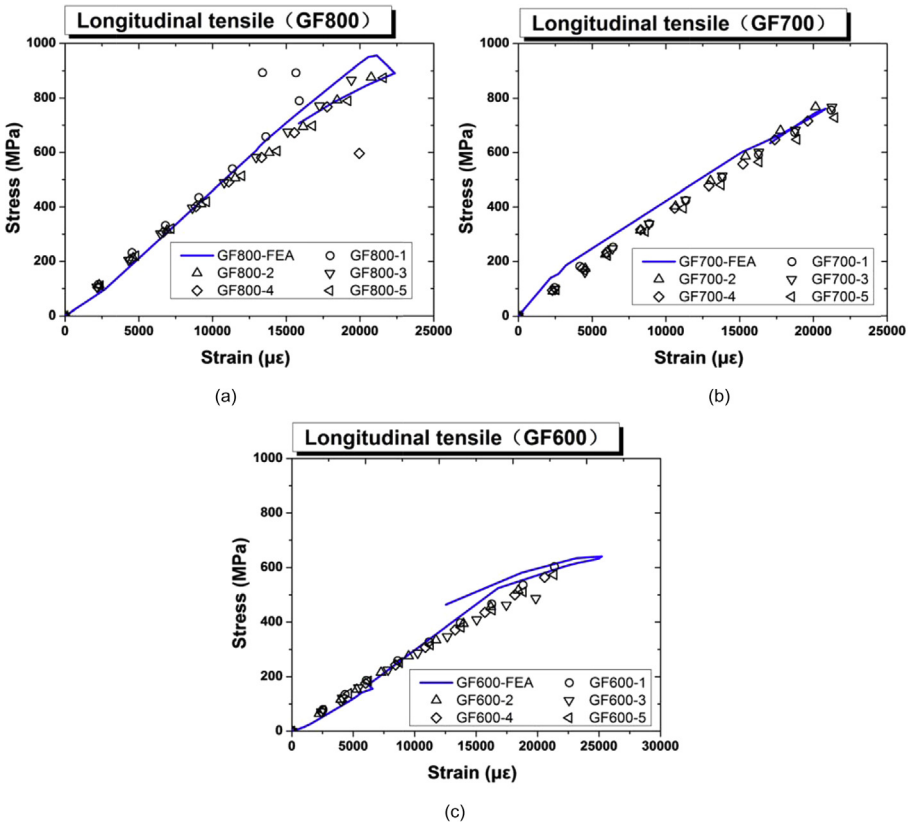

Fig. 16. Comparision between numerical and experimental longitudinal tensile stress–strain relationship.

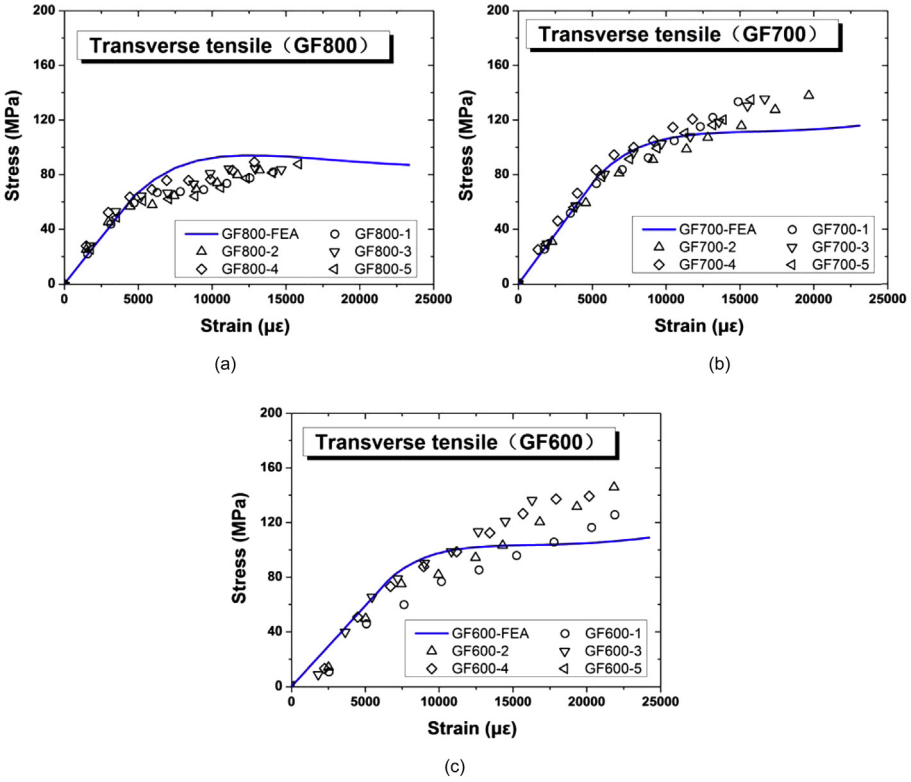

Fig. 17. Comparision between numerical and experimental transverse tensile stress–strain relationship.

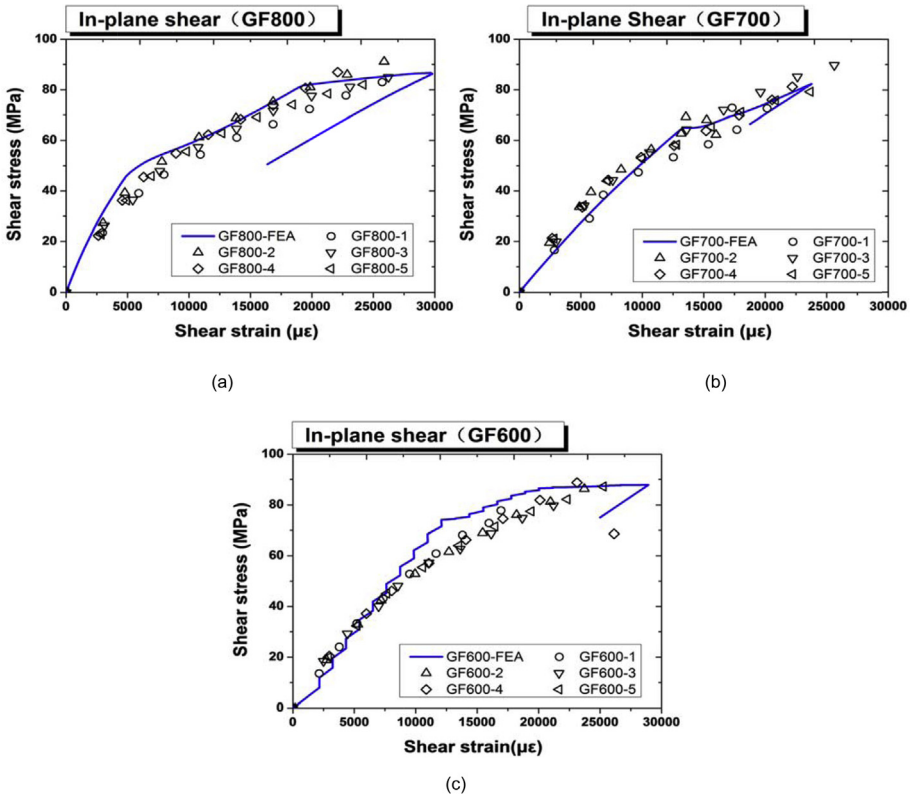

Fig. 18. Comparision between numerical and experimental in-plane shear stress-shear strain relationship.

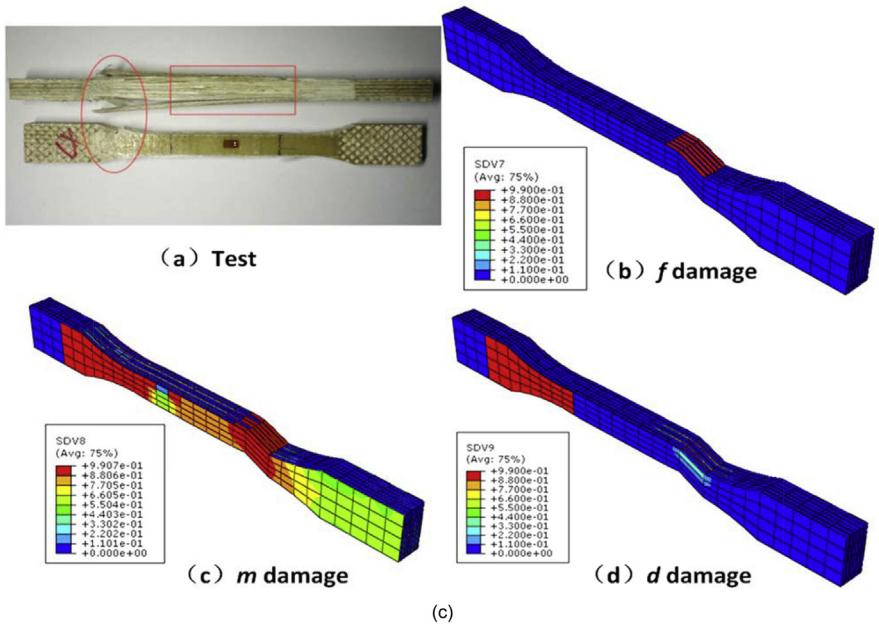

Fig. 19. Comparison between numerical and experimental longitudinal tensile failure modes.

expected in the future. The maximum damage variable d_{max} (in Fig. 13) is assumed to be 0.999 to avoid the values of element stiffness matrix to be zero causing convergence problems.

The comparison of numerical ultimate capacity and test results is shown in Fig. 15. It is shown that the difference between numerical strength and average test results is within 10% except transverse tensile strength of GF700 and GF600, indicating the theoretical results agreed well with test results. The stress–strain relationship comparisons between numerical and test results were shown in Figs. 16–18. A good agreement could be observed in lon-

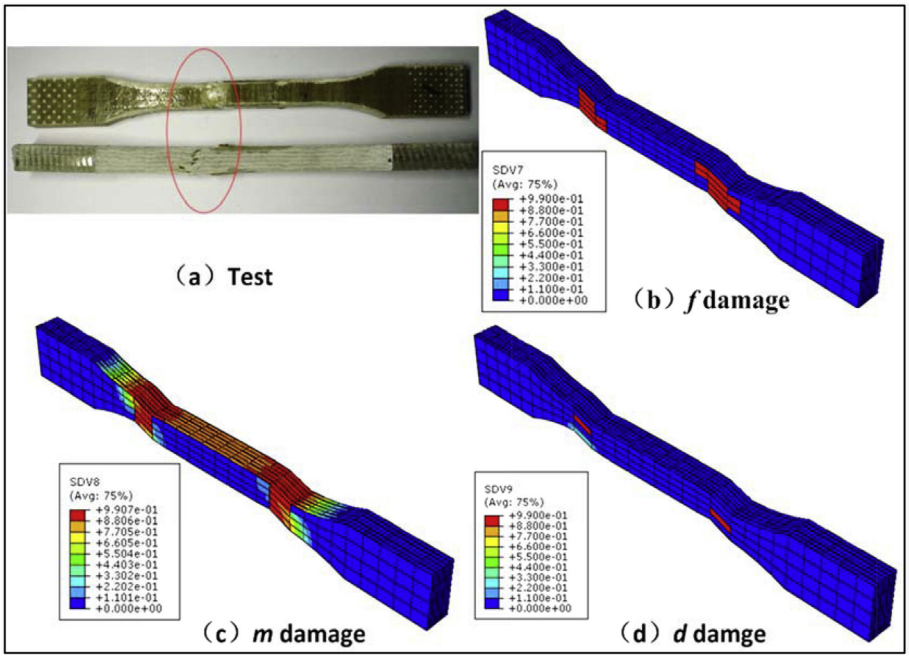

Fig. 20. Comparison between numerical and experimental transverse tensile failure modes.

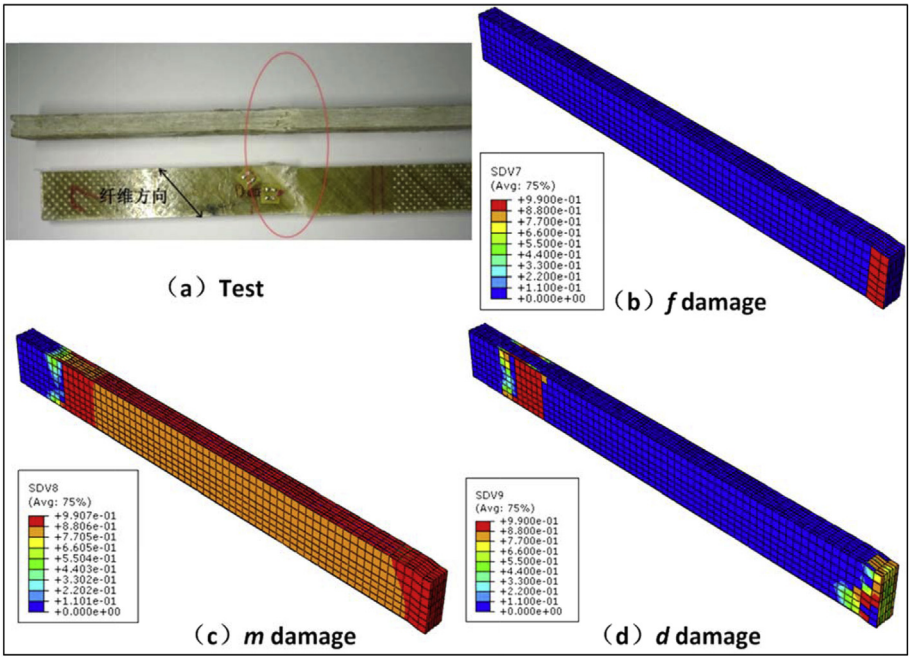

Fig. 21. Comparison between numerical and experimental in-plane shear failure modes.

gitudinal tensile stress–strain curve, transverse tensile stress–strain curve and in-plane shear stress- strain curve. Failure modes comparisons between numerical and test results were shown in Fig. 19 through Fig. 21. The experimental failure modes agreed well with numerical failure modes, and the cracks area are accorded with the fully damaged area ($d = d_{max}$).

6. Conclusions

In order to extend the use of pultruded GFRP materials in civil engineering, a systematic study on material properties of GFRP profiles is important and realistic for the design and construction of GFRP structures in bridge engineering. The following conclusions can be drawn from present study:

(1) The average test value, test value with 95% guaranteed rate, suggested design value by MOHURD GB50608-2010 and ASCE-MOP 102 of longitudinal and transverse elastic modulus, shear modulus, longitudinal and transverse tensile strength and shear strength of three different laminates are determined in this paper based on material experiments.

(2) The difference between theoretical engineering constants and average test results is within 10%, indicating the theoretical results agreed well with test results. The difference of longitudinal elastic modulus and shear modulus between theoretical and suggested design value by MOHURD GB50608-2010 [27] is within 5%, while the difference between theoretical and suggested transverse elastic modulus by MOHURD GB50608-2010 [27] is 10%. The difference of longitudinal elastic modulus and shear modulus between theoretical and suggested design value by ASCE-MOP 102 [28] is almost 10%, while the transverse elastic modulus difference between theoretical and suggested design value by ASCE-MOP 102 [28] is almost 20%.

(3) To simplify the design process, the innovative multi carpet plots with fiber fraction from 20% to 75% is proposed in this paper. The multi carpet plots allow designers to preliminary design and predict the engineering constants of GFRP laminate without complicated calculation.

(4) A continuum damage model considering shear nonlinearity, lamina damage along thickness direction, innovative damage evaluation methods, loading/unloading strategy and viscous methods to alleviate the convergence difficulties is proposed and implemented via user material subroutine. The FE simulation results are validated with tests and could provide reference for the design and construction of GFRP structures.

Acknowledgments

The authors gratefully acknowledge the financial support provided by National Natural Science Foundation [Grant # 51578406] of People's Republic of China.

References

[1] Mosallam AS, Bayraktar A, Elmikawi M, Pul S, Adanur S. Polymer composites in construction: an overview. SOJ Mater Sci Eng 2015;2(1):25, Open Access.
[2] Mosallam AS. Composites in construction. Chapter 45. Materials selection handbook, vol. 53. NY, USA: John Wiley Publishing Co; 2002.
[3] Ascione L, Caron JF, Godonou P, van IJselmuijden K, Knippers J, Mottram T, Ellipsis, Tromp L. Prospect for new guidance in the design of FRP: Support to the implementation, harmonization and further development of the Eurocodes. Publications Office of the European Union; 2016.
[4] He J, Liu YQ, Chen AR, Dai L. Experimental investigation of movable hybrid GFRP and concrete bridge deck. Constr Build Mater 2012;26(1):49–64.
[5] Xin H, Liu Y, He J, Fan H, Zhang Y. Fatigue behavior of hybrid GFRP-concrete bridge decks under sagging moment. Steel Compos Struct 2015;18(4):925–46.
[6] Xin H, Liu Y, Du A. Thermal analysis on composite girder with hybrid GFRP-concrete deck. Steel Compos Struct 2015;19(5):1221–36.
[7] Mosallam AS, Feo L, Elsadek A, Pul S, Penna R. Structural evaluation of axial and rotational flexibility and strength of web-flange junctions of open-web pultruded composites. Compos B Eng 2014;66:311–27.
[8] Ascione F, Feo L, Maceri F. An experimental investigation on the bearing failure load of glass fibre/epoxy laminates. Compos B Eng 2009;40(3):197–205.
[9] Ascione F, Mancusi G. The influence of the web-flange junction stiffness on the mechanical behaviour of thin-walled pultruded beams. Compos B Eng 2013;55:599–606.
[10] Feo L, Mosallam AS, Penna R. Mechanical behavior of web-flange junctions of thin-walled pultruded I-profiles: an experimental and numerical evaluation. Compos B Eng 2013;48:18–39.
[11] Xin H, Mosallam A, Liu Y, Yang F, Zhang Y. Hygrothermal aging effects on shear behavior of pultruded FRP composite web-flange junctions in bridge application. Compos B Eng 2017;110:213–28.
[12] Xin H, Mosallam A, Liu Y, Wang C, Zhang Y. Impact of hygrothermal aging on rotational behavior of web-flange junctions of structural pultruded composite members for bridge applications. Compos B Eng 2017;110:279–97.
[13] Ascione F, Feo L, Maceri F. On the pin-bearing failure load of GFRP bolted laminates: an experimental analysis on the influence of bolt diameter. Compos B Eng 2010;41(6):482–90.
[14] Ascione F. A preliminary numerical and experimental investigation on the shear stress distribution on multi-row bolted FRP joints. Mech Res Commun 2010;37(2):164–8.
[15] Xin H, Liu Y, Mosallam A, Zhang Y, Wang C. Hygrothermal aging effects on flexural behavior of pultruded glass fiber reinforced polymer laminates in bridge applications. Constr Build Mater 2016;127:237–47.
[16] Xin H, Mosallam A, Liu Y, Wang C, Zhang Y. Analytical and experimental evaluation of flexural behavior of FRP pultruded composite profiles for bridge deck structural design. Constr Build Mater 2017;150:123–49.
[17] Xin H, Mosallam A. Liu, etc, Experimental andNumerical Investigation on In-Plane Compression and Shear Performance of a Pultruded GFRP Composite BridgeDeck. Compos Struct 2017;180:914–32. https://doi.org/10.1016/j.compstruct.2017.08.066.
[18] Du A, Liu Y, Xin H, Zuo Y. Progressive damage analysis of PFRP double-lap bolted joints using explicit finite element method. Compos Struct 2016;152:860–9.
[19] Feo L, Marra G, Mosallam AS. Stress analysis of multi-bolted joints for FRP pultruded composite structures. Compos Struct 2012;94(12):3769–80.
[20] Uddin N (Ed.). Developments in fiber-reinforced polymer (FRP) composites for civil engineering. Elsevier; 2013.
[21] Soden PD, Hinton MJ, Kaddour AS. Lamina properties, lay-up configurations and loading conditions for a range of fibre-reinforced composite laminates. Compos Sci Technol 1998;58(7):1011–22.
[22] Barbero EJ. Introduction to composite materials design. CRC Press; 2010.
[23] Liu L, Huang ZM. Stress concentration factor in matrix of a composite reinforced with transversely isotropic fibers. J Compos Mater 2014;48(1):81–98.
[24] Weeton JW, Thomas KL, Peters DM. Engineers' guide to composite materials. American Society of Metals; 1987.
[25] Stellbrink KK. Micromechanics of composites: composite properties of fibre and matrix constituents (Vol. 1). Hanser Gardner Pubns; 1996.
[26] ISO, B. 527–4. Plastics–determination of tensile properties–part 4: test conditions for isotropic and orthotropic fibre-reinforced plastic composites. International Organization for Standardization (ISO), Geneva, Switzerland, 1997.
[27] ISO, B. 14129. Fibre-reinforced plastic composites– Determination of the in-plane shear stress/shear strain response, including the in-plane shear modulus and strength, by the±45 tension test method. International Organization for Standardization (ISO), Geneva, Switzerland, 1997.
[28] Ministry of housing and urban-rural development of the People's Republic of China (MOHURD GB50608). Technical code for infrastructure application of FRP composites. GB50608-2010 Beijing, China: China Planning Press; 2011(In Chinese).
[29] Mosallam AS. Design guide for FRP composite connections, ASCE manuals and reports on engineering practice MOP#102. Reston, Virginia, USA: American Society of Civil Engineers (ASCE); 2011, ISBN 9780784406120.
[30] Huang ZM Zhou YX. Strength of fibrous composites. Springer press; 2011.
[31] ABAQUS V. 6.14 documentation. Dassault Systemes Simulia Corporation; 2014.
[32] Chow CL, Wang J. An anisotropic theory of elasticity for continuum damage mechanics. Int J Fract 1987;33(1):3–16.
[33] Liu Y, Filonova V, Hu N, et al. A regularized phenomenological multiscale damage model. Int J Numer Meth Eng 2014;99(12):867–87.
[34] Hahn HT, Tsai SW. Nonlinear elastic behavior of unidirectional composite laminae. J Compos Mater 1973;7(1):102–18.
[35] Sidoroff F. Description of anisotropic damage application to elasticity[M]// Physical Non-Linearities in Structural Analysis. Berlin Heidelberg: Springer; 1981. p. 237–44.
[36] Hashin Z. Failure criteria for unidirectional fiber composites. J Appl Mech 1980;47(2):329–34.
[37] Liu P, Cheng X, Wang S, Liu S, Cheng Y. Numerical analysis of bearing failure in countersunk composite joints using 3D explicit simulation method. Compos Struct 2016;138:30–9.
[38] Lapczyk I, Hurtado JA. Progressive damage modeling in fiber-reinforced materials. Compos A Appl Sci Manuf 2007;38(11):2333–41.
[39] Yuan Z, Fish J. Are the cohesive zone models necessary for delamination analysis? Comput Methods Appl Mech Eng 2016;310:567–604.
[40] Duvant G, Lions JL. Inequalities in mechanics and physics. Springer Science & Business Media, 2012.